

CHEMICAL COMMUNICATIONS

Evaporative self-assembly of single-chain, polymeric nanoparticles

Hendrik W. H. van Roekel,^{a,b} Patrick J. M. Stals,^{a,c} Martijn A. J. Gillissen,^{a,c}
Peter A. J. Hilbers,^{a,b} Albert J. Markvoort*^{a,b} and Tom F. A. de Greef*^{a,b,c}

^a*Institute for Complex Molecular Systems, Eindhoven University of Technology,
P.O. Box 513, 5600 MB Eindhoven, The Netherlands. E-mail:
a.j.markvoort@tue.nl, t.f.a.d.greef@tue.nl*

^b*Computational Biology group, Eindhoven University of Technology*

^c*Laboratory of Macromolecular and Organic Chemistry, Eindhoven University
of Technology*

ELECTRONIC SUPPLEMENTARY INFORMATION

Two-dimensional Monte Carlo model

The lattice-gas model developed by Rabani [1] is used here to rationalize the observed morphologies as measured by atomic force microscopy (AFM). First, it is assumed that the relevant processes governing evaporative self-assembly of polymeric nanoparticles can be captured in a two-dimensional model, thus neglecting any changes in film-thickness. Second, it is assumed that all relevant dynamics arise from the diffusion of nanoparticles and evaporation of the solvent. These assumptions have proven to be adequate in understanding the formation of polygonal networks and spinodal structures of inorganic nanoparticles resulting from the dewetting of an ultrathin liquid film that remains behind the mesoscopic dewetting front, where the nanoparticles are regarded as a two-dimensional subsystem [2-4]. At an initial diameter of ~10 nm, globular polymeric nanoparticles are comparable in size to inorganic nanoparticles [5,2-4], so their diffusive properties ought to be similar. For a film-thickness equal to or below 10 nm and about equal to nanoparticle thickness, convective transport of the solution can be neglected [4]. The height of the polymeric nanoparticle after evaporation [5] is lower than 10 nm. Furthermore, intermolecular interactions between polymeric nanoparticles are not 'sticky', allowing association and dissociation of diffusing particles. And finally, through AFM, single layers of polymeric nanoparticles are measured. Therefore, the aforementioned assumptions underlying the Monte Carlo model seem very reasonable for our systems with polymeric nanoparticles as well.

Hamiltonian

The Monte Carlo model utilizes a Hamiltonian which defines the interactions between adjacent lattice cells and takes into account the chemical potential, μ . We define a square lattice, where a single lattice cell i , can be occupied by solvent, either in the liquid state of matter ($l_i = 1, n_i = 0$) or in the gaseous state of matter ($l_i = 0, n_i = 0$), or by a part of a nanoparticle ($l_i = 0, n_i = 1$). A polymeric nanoparticle is represented by 3×3 lattice cells, and will keep this shape throughout the simulation. An illustration of the computational grid is depicted in figure S1. Assuming that the interaction between two liquid particles, two nanoparticles or between a liquid particle and a nanoparticle is much higher than any interaction with gas, three interaction terms are introduced. The liquid-liquid interaction term ε_{ll} reflects interactions between liquid lattice cells, the nanoparticle-nanoparticle interaction term ε_{nn} reflects adhesive interactions between nanoparticles and liquid particles, and the nanoparticle-liquid interaction term ε_{nl} reflects the adhesive interactions between the nanoparticles. Furthermore, the solvent in the liquid phase has a chemical potential, μ_1 , which is higher than the chemical potential of the solvent in the gas phase, μ_2 . Solvent molecules tend to move from areas of higher chemical potential to lower chemical potential [6]. Polymeric nanoparticles follow random walk statistics, meaning that a nanoparticle can move in all directions with equal probability. The Hamiltonian of the system can now be written as in equation (S1).

$$H = -\varepsilon_{ll} \sum_{\langle ij \rangle} l_i l_j - \varepsilon_{nl} \sum_{\langle ij \rangle} n_i l_j - \varepsilon_{nn} \sum_{\langle ij \rangle} n_i n_j - \mu \sum_i l_i \quad (\text{S1})$$

Here, $\langle ij \rangle$ indicates summation over nearest neighbour interactions and μ is the effective chemical potential comprising both the liquid-gas chemical potential $\mu_2 - \mu_1$ and the homogeneous interaction of liquid with the substrate [7].

In the computational implementation, we first define the entire lattice as L . If a certain lattice cell i represents solvent in the gas phase, $L_i = 0$, if it represents solvent in the liquid phase, $L_i = 1$, and if it represents a single lattice cell of a 3×3 nanoparticle, $L_i = 2$. With the lattice matrix defined, the Hamiltonian can now be written in terms of L as depicted in equation (S2).

$$H = -\varepsilon_{ll} \sum_{\langle ij \rangle} \delta_{L_j,1} \delta_{L_i,1} - \varepsilon_{nl} \left(\sum_{\langle ij \rangle} \delta_{L_i,1} \delta_{L_j,2}^\Omega + \sum_{\langle ij \rangle} \delta_{L_i,2}^\Omega \delta_{L_j,1} \right) - \varepsilon_{nm} \sum_{\langle ij \rangle} \delta_{L_i,2}^\Omega \delta_{L_j,2}^\Omega - \mu \sum_i \delta_{L_i,1} \quad (\text{S2})$$

In equation (S2), $\delta_{a,b}$ represents the Kronecker delta, and the summations run over two adjacent lattice cells: the one on the right and the one below the current lattice cell i . This avoids counting interactions twice. Our simulations employ periodic boundary conditions, that is, cells on the boundary of the lattice have interactions with cells on the other side of the lattice. Lastly, L_i^Ω indicates that a lattice cell on the edge of a 3×3 nanoparticle is considered.

Next-nearest neighbour Hamiltonian

In order to obtain more realistic simulation results, Moriarty and coworkers [8] introduced the use of next-nearest neighbour interactions when calculating the energy change upon a solvent transition or diffusion step. Particularly, it was shown that the inclusion of these next-nearest neighbour interactions, scaled with $\frac{1}{\sqrt{2}}$ to reflect a linear decay in interaction strength with distance, resulted in an increased isotropy in the evaporation of the solvent [2-4,7-11]. Hence, the Hamiltonian becomes (S3):

$$H = \frac{\sqrt{2}}{1 + \sqrt{2}} \left[-\varepsilon_{ll} \sum_{\langle ij \rangle} \delta_{L_j,1} \delta_{L_i,1} - \varepsilon_{nl} \left(\sum_{\langle ij \rangle} \delta_{L_i,1} \delta_{L_j,2}^\Omega + \sum_{\langle ij \rangle} \delta_{L_i,2}^\Omega \delta_{L_j,1} \right) - \varepsilon_{nm} \sum_{\langle ij \rangle} \delta_{L_i,2}^\Omega \delta_{L_j,2}^\Omega + \right. \\ \left. - \frac{1}{\sqrt{2}} \left(\varepsilon_{ll} \sum_{\langle ik \rangle} \delta_{L_k,1} \delta_{L_i,1} + \varepsilon_{nl} \left(\sum_{\langle ik \rangle} \delta_{L_i,1} \delta_{L_k,2}^\Omega + \sum_{\langle ik \rangle} \delta_{L_i,2}^\Omega \delta_{L_k,1} \right) + \varepsilon_{nm} \sum_{\langle ik \rangle} \delta_{L_i,2}^\Omega \delta_{L_k,2}^\Omega \right) \right] - \mu \sum_i \delta_{L_i,1} \quad (\text{S3})$$

Renormalization of $\frac{\sqrt{2}}{1 + \sqrt{2}}$ is introduced to provide a similar global energy for the next-nearest neighbour model as for the original, nearest neighbour model in equation (S2), where $\langle ij \rangle$ indicates summation over the adjacent cells of current cell i (to the right and below) and $\langle ik \rangle$ indicates summation over the bottom right and bottom left cells of current cell i .

Local Hamiltonian differences

Simulations start with a lattice that is initially covered with randomly placed nanoparticles and further filled with liquid solvent. Updates are performed using the Metropolis algorithm [12], where a single Monte Carlo step is defined such that in expectation, each solvent cell is considered once for evaporation or condensation, and each nanoparticle is considered a certain number of times (MR , the mobility ratio) for diffusion in one of the directions left, right, up or down [1-4,7-10]. Upon a local move not the entire Hamiltonian needs to be recalculated, instead ΔH can be calculated locally. Figure S2 depicts a solvent cell $L_{i,j}$ under consideration for evaporation or condensation and the lattice cells which are used in determining the change in the Hamiltonian, ΔH . Note the two-dimensional notation $L_{i,j}$, for ease of evaluating local Hamiltonian differences. If the considered solvent cell is in the liquid phase, the local change of the Hamiltonian is defined in equation (S4).

$$\begin{aligned} \Delta H_{\text{evap}} = & \frac{\sqrt{2}}{1+\sqrt{2}} \left[\varepsilon_{ll} (\delta_{L_{i-1,j},1} + \delta_{L_{i,j-1},1} + \delta_{L_{i+1,j},1} + \delta_{L_{i,j+1},1}) + \varepsilon_{nl} (\delta_{L_{i-1,j},2} + \delta_{L_{i,j-1},2} + \delta_{L_{i+1,j},2} + \delta_{L_{i,j+1},2}) + \right. \\ & \left. + \frac{1}{\sqrt{2}} \{ \varepsilon_{ll} (\delta_{L_{i-1,j+1},1} + \delta_{L_{i,j+1},1} + \delta_{L_{i+1,j+1},1} + \delta_{L_{i,j+1},1}) + \varepsilon_{nl} (\delta_{L_{i-1,j+1},2} + \delta_{L_{i,j+1},2} + \delta_{L_{i+1,j+1},2} + \delta_{L_{i,j+1},2}) \} \right] + \mu \end{aligned} \quad (\text{S4})$$

If this solvent cell is in the gas phase, the change is $\Delta H_{\text{cond}} = -\Delta H_{\text{evap}}$. Figure S3 displays a nanoparticle in a graphical 7×7 submatrix S and shows the affected nearest neighbour and next-nearest neighbour lattice sites when the particle would move upward. The associated change in Hamiltonian upon movement of the nanoparticle in the upward direction using nearest and next-nearest neighbour interactions can now be expressed as in equation (S5). The derivation is similar for the movement of a nanoparticle into the other directions, except that other lattice cells in S should be considered.

$$\begin{aligned} \Delta H = & \frac{\sqrt{2}}{1+\sqrt{2}} \left[(\varepsilon_{ll} - \varepsilon_{nl}) (\delta_{S_{1,3},1} + \delta_{S_{1,4},1} + \delta_{S_{1,5},1} + \delta_{S_{2,2},1} + \delta_{S_{2,6},1}) + \right. \\ & + (\varepsilon_{nl} - \varepsilon_{nn}) (\delta_{S_{1,3},2} + \delta_{S_{1,4},2} + \delta_{S_{1,5},2} + \delta_{S_{2,2},2} + \delta_{S_{2,6},2}) + \\ & + (\varepsilon_{nl} - \varepsilon_{ll}) (\delta_{S_{6,3},1} + \delta_{S_{6,4},1} + \delta_{S_{6,5},1} + \delta_{S_{5,2},1} + \delta_{S_{5,6},1}) + \\ & + (\varepsilon_{nn} - \varepsilon_{nl}) (\delta_{S_{6,3},2} + \delta_{S_{6,4},2} + \delta_{S_{6,5},2} + \delta_{S_{5,2},2} + \delta_{S_{5,6},2}) + \\ & + \frac{1}{\sqrt{2}} \{ (\varepsilon_{ll} - \varepsilon_{nl}) (\delta_{S_{1,2},1} + \delta_{S_{1,3},1} + 2\delta_{S_{1,4},1} + \delta_{S_{1,5},1} + \delta_{S_{1,6},1} + \delta_{S_{3,2},1} + \delta_{S_{3,6},1}) + \\ & + (\varepsilon_{nl} - \varepsilon_{nn}) (\delta_{S_{1,2},2} + \delta_{S_{1,3},2} + 2\delta_{S_{1,4},2} + \delta_{S_{1,5},2} + \delta_{S_{1,6},2} + \delta_{S_{3,2},2} + \delta_{S_{3,6},2}) + \\ & + (\varepsilon_{nl} - \varepsilon_{ll}) (\delta_{S_{6,2},1} + \delta_{S_{6,3},1} + 2\delta_{S_{6,4},1} + \delta_{S_{6,5},1} + \delta_{S_{6,6},1} + \delta_{S_{4,2},1} + \delta_{S_{4,6},1}) + \\ & \left. + (\varepsilon_{nn} - \varepsilon_{nl}) (\delta_{S_{6,2},2} + \delta_{S_{6,3},2} + 2\delta_{S_{6,4},2} + \delta_{S_{6,5},2} + \delta_{S_{6,6},2} + \delta_{S_{4,2},2} + \delta_{S_{4,6},2}) \} \right] \end{aligned} \quad (\text{S5})$$

A move (i.e. diffusion, condensation or evaporation) is accepted with the Metropolis acceptance probability P_{acc} as given in equation (S6).

$$P_{\text{acc}} = \min \left(1, e^{-\frac{\Delta H}{kT}} \right) \quad (\text{S6})$$

Here, T is the temperature and k is the Boltzmann constant. If the lattice contains N^2 cells and n nanoparticles ($9n < N^2$), the Metropolis algorithm for a single Monte Carlo (MC) step in the simulations is now summarized as follows:

- 1) Diffusion of nanoparticles is done first, the following steps are repeated $MR \times n$ times:
 1. Randomly select a nanoparticle in the lattice.
 2. Choose a direction into which it will move with probability 0.25 (up, down, left or right).
 3. If the chosen direction has three liquid cells filled adjacent to the nanoparticle, determine ΔH using equation (S5), if not, this trial move is rejected.
 4. If step three is successful, accept the move using the Metropolis acceptance probability in equation (S6).
- 2) Then, phase change of solvent is considered, the following steps are repeated $N^2 - 9n$ times:
 1. Randomly select a solvent cell in the lattice.
 2. If the solvent cell is liquid, determine ΔH_{evap} as in equation (S4), if the solvent cell is gas, determine $\Delta H_{\text{cond}} = -\Delta H_{\text{evap}}$.
 3. Change the state of matter of the solvent lattice cell using the Metropolis acceptance probability in equation (S6).

Depending on the type of simulation – which is a direct result of the choice of the interaction parameters, the effective chemical potential and the temperature – 500 to 20,000 MC steps are required for most solvent cells to turn into vapour. The model is capable of simulating self-assembly processes driven by nucleated and spinodal dewetting [1-4,7-10]. Furthermore, the two-dimensional Monte Carlo model can be transformed in a pseudo three-dimensional model by expressing the effective chemical potential as a function of the vapour fraction [6,7,3]. In this work, simulations are performed in the early spinodal regime. In the early spinodal regime, we choose the effective chemical potential such that when we map the system onto an Ising lattice, there is no external magnetic field, i.e. $\mu \approx -2\varepsilon_{ll} - 2\phi(\varepsilon_{nl} - \varepsilon_{ll})$, and the temperature is near the critical temperature $kT \approx kT_c^\infty \approx 0.57\varepsilon_{ll}$ [4].

Experimental

The poly(methyl methacrylate) (PMMA) polymer has a number averaged molecular weight $M_n = 67900$ g/mol and a polydispersity index of 1.43 as measured using gel permeation chromatography (GPC, CHCl_3 /polystyrene standards). On average, the polymer has 47 ureido-pyrimidinone (UPy) groups per chain. Details of the synthesis and physical characterization of the folding of this polymer using GPC and dynamic light scattering (DLS) are discussed elsewhere [13]. In short, detailed DLS measurements confirm that the polymer has a globular shape after deprotection of the protected UPy groups. Solvents used during measurements were of AR quality or better and obtained from Biosolve. Atomic force micrographs were recorded under ambient conditions with silicon cantilever tips (PPP-NCH, 300-330 kHz, 42 N/m from Nanosensors) using an Asylum Research MFP-3D-Bio in non-contact mode. Samples were prepared in two different ways. For the sample with ~60% coverage (figure S5), a drop of a 0.01 mg/mL solution of polymer in dioxane was spincoated on a freshly cleaved mica surface (grade V1, Ted Pella Inc.) at 2500 rpm for 60 seconds. The samples with ~0.17% (figure S4) coverage and ~90% (figure S6)

coverage were obtained by dropcasting 5 μL of a 0.0025 mg/mL solution of polymer in dioxane ($\sim 0.17\%$ coverage) and 10 μL of 0.05 mg/mL solution of polymer in dioxane ($\sim 90\%$ coverage) on a freshly cleaved mica surface (grade V1, Ted Pella Inc.) after which the sample was allowed to equilibrate for 3 days in a solvent chamber filled with dioxane. All samples were measured at different positions on the surface of each sample and in all cases comparable topologies were observed on each position. Images were processed using Scanning Probe Image Processor software (Image Metrology A/S).

Image analysis

The AFM height images were subjected to image preprocessing steps. The images were converted to binary images using a threshold determined using Otsu's method [14,15], so that the percentage of coverage of nanoparticles could be estimated. When necessary, noise was reduced in the binary images using median filtering [14]. This noise reduction was sometimes necessary in order for germs used in the Minkowski functional grain growth analysis [8,16] (*vide infra*) to be placed automatically on particles or in holes, i.e. at their centroids. Figure S7 (a), (b) and (c) display the binary images of an AFM height image and figure S7 (d), (e) and (f) display the original grey-scale images with the germs derived from the binary image, each at increasing coverage respectively (0.17%-60%-90%).

For simulated images, binary images were obtained by multiplying all components of the matrix L by 0.5 and thresholding the resulting matrix at 0.5. All components in the matrix $0.5L$ that are larger than 0.5 represent nanoparticles in the simulation, and hence the thresholded matrix represents the final simulation morphology. Median filtering was required for the images corresponding to 60% and 90% coverage, in order to remove artifacts (i.e. small holes) from the simulations.

Computational morphologies were obtained using the nanoparticle coverage found from analysis of the experimental AFM images. Different simulated morphologies were obtained by varying the mobility ratio (MR), the temperature and the chemical potential. The simulated morphologies were subjected to a Minkowski functional grain growth analysis [16] and the computed morphologies showing the best correspondence to the experimental images are presented in the main text.

Minkowski functional grain growth analysis

The Minkowski functionals – i.e. the total area of white pixels A , the total perimeter of white pixels U and the Euler characteristic χ – can be calculated for all images as a function of r , where $2r + 1$ is the square grain side length. The principle is outlined in figure 3 of the main text. As the number of pixels in the images is likely to differ, these functionals are made independent of the image size by normalization and plotting them against the normalized distance. The normalized Minkowski functionals are defined as (S7) [16]

$$A^* = \rho \frac{A}{M}, U^* = \sqrt{\rho} \frac{U}{M}, \chi^* = \frac{\chi}{M} \quad (\text{S7})$$

where M represents the number of germs in the image and $\rho = \frac{M}{N^2}$ is the germ density in the image having N^2 pixels. The deviation from the expected normalized Minkowski functionals constructed for a random point set gives an indication whether the germ distribution on the image is the result of a physical mechanism, or the result of chance alone [16, 17]. The expected normalized Minkowski functionals for growing square grains from random germs are defined as (S8)

$$\begin{aligned}\langle A^* \rangle &= 1 - e^{-\rho a^2} \\ \langle U^* \rangle &= 4a\sqrt{\rho}e^{-\rho a^2} \\ \langle \chi^* \rangle &= (1 - \rho a^2)e^{-\rho a^2}\end{aligned}\quad (\text{S8})$$

with $a = 2r + 1$ [16]. To compare the calculated normalized Minkowski measures with their matching expectation for a random point set, we need to express the functionals as a function of the normalized distance x between germs, again to account difference in image sizes. The normalized distance is defined as $x = \frac{r}{s_{\text{mean}}}$, where s_{mean} is the mean separation distance, defined as (S9)

$$s_{\text{mean}} = \frac{1}{M} \sum_{i=1}^M \min_{i \neq j} (D_{ij}) \quad (\text{S9})$$

where D is an $M \times M$ matrix containing all distances between all germs and M is the number of germs in the image. For every germ i taken as a reference, we need the distance to its closest germ, which is why we take the minimum of all distances to all other germs, j . The mean separation distance is calculated by taking the mean of these closest distances. All of the resulting Minkowski grain growth analyses are depicted in figures S8-S10. As can be observed, there is a strong resemblance in all Minkowski functionals between the experimental and computed morphologies for all three images.

References

- [1] E. Rabani, D. R. Reichman, P. L. Geissler and L. E. Brus, *Nature*, 2003, **426**, 271
- [2] U. Thiele, I. Vancea, A. J. Archer, M. J. Robbins, L. Frastia, A. Stannard, E. Pauliac-Vaujour, C. P. Martin, M. O. Blunt and P. J. Moriarty, *J. Phys.: Condens. Matter*, 2009, **21**, 264016
- [3] E. Pauliac-Vaujour, A. Stannard, C. P. Martin, M. O. Blunt, I. Notingher P. J. Moriarty, I. Vancea and U. Thiele, *Phys. Rev. Lett.*, 2008, **100**, 176102
- [4] I. Vancea, U. Thiele, E. Pauliac-Vaujour, A. Stannard, C. P. Martin, M. O. Blunt and P. J. Moriarty, *Phys. Rev. E*, 2008, **78**, 041601
- [5] E. B. Berda, E. J. Foster, and E. W. Meijer, *Macromolecules*, 2010, **43**, 1430

- [6] R. Baierlein, *Am. J. Phys.*, 2001, **69**, 423
- [7] A. Stannard, C. P. Martin, E. Pauliac-Vaujour, P. J. Moriarty and U. Thiele, *J. Phys. Chem. C*, 2008, **112**, 15195
- [8] C. P. Martin, M. O. Blunt and P. J. Moriarty, *Nano Lett.*, 2004, **4**, 2389
- [9] C. P. Martin, M. O. Blunt, E. Pauliac-Vaujour, A. Stannard, P. J. Moriarty, I. Vancea and U. Thiele, *Phys. Rev. Lett.*, 2008, **99**, 116103
- [10] A. Stannard, *J. Phys.: Condens. Matter*, 2011, **23**, 083001
- [11] G. Yosef and E. Rabani, *J. Phys. Chem. B*, 2006, **110**, 20965
- [12] N. Metropolis, A. W. Rosenbluth, M. N. Rosenbluth, A. H. Teller and E. Teller, *J. Chem. Phys.*, 1953, **21**, 1087
- [13] P. J. M. Stals, M. A. J. Gillissen, R. Nicolaÿ, A. R. A. Palmans and E. W. Meijer, *Polym. Chem.*, 2013, DOI:10.1039/C3PY00094J
- [14] R. C. Gonzalez, R. E. Woods and S. L. Eddins, *Digital Image Processing Using Matlab®*, Second Edition, Gatesmark Publishing, 2009, ISBN: 978-0-9820854-0-0
- [15] N. Otsu, *IEEE Trans., Sys., Man., Cyber.*, 1979, **9**, 62
- [16] K. Michielsen and H. De Raedt, *Phys. Rep.*, 2001, **347**, 461
- [17] F. Frehill, K. H. G. Schulte, C. P. Martin, L. Wang, S. Patel, J. A. Purton, J. G. Vos and P. J. Moriarty, *Langmuir*, 2004, **20**, 6421

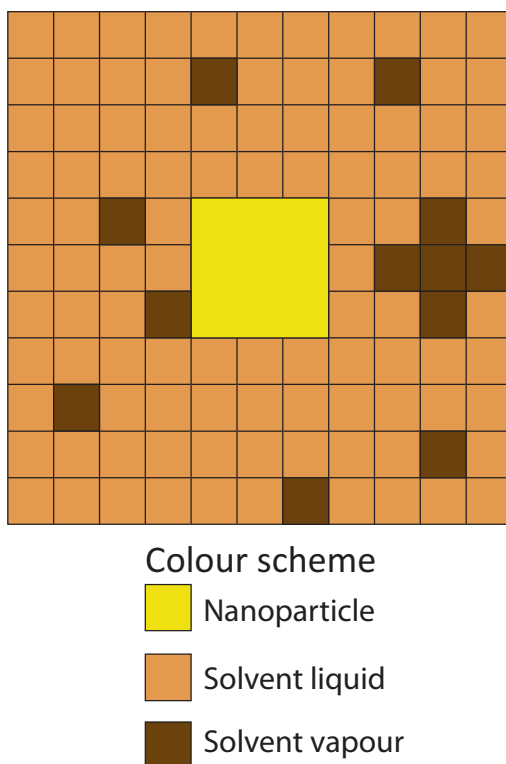
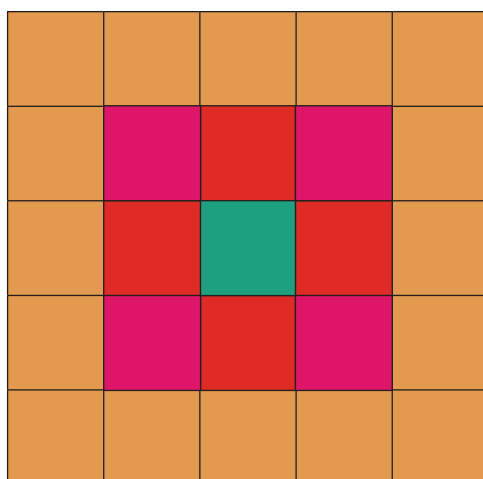


Fig. S1 A colour scheme representation of a lattice (11×11) containing solvent, gas and nanoparticle cells. In this configuration, the nanoparticle is unable to move to the left, as one of the neighbouring cells is in a gaseous state.



Colour scheme



Considered solvent cell

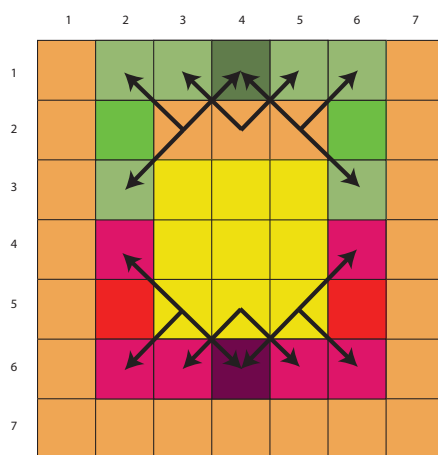


Affected nearest neighbours



Affected next-nearest neighbours

Fig. S2 A solvent cell under consideration (turquoise) with its nearest neighbouring lattice cells (red) and next-nearest neighbouring lattice cells (purple) relevant for the evaluation of the Hamiltonian difference upon solvent evaporation/condensation.



Colour scheme

-  Formed nearest neighbour interactions with 3x3 nanoparticle upon upward movement
-  Broken nearest neighbour interactions with 3x3 nanoparticle upon upward movement
-  Formed next-nearest neighbour interactions with 3x3 nanoparticle upon upward movement
-  Broken next-nearest neighbour interactions with 3x3 nanoparticle upon upward movement

Fig. S3 Diffusion of a nanoparticle in the upward direction on a sublattice *S*: Diffusion results in the loss of the interactions with the next-nearest neighbour lattice sites indicated in purple, and new interactions are formed with the next-nearest neighbour lattice sites indicated in turquoise. Conversely, the liquid lattice cells lose next-nearest neighbour interactions with the lattice cells indicated in turquoise, and forms new interactions with the next-nearest neighbouring lattice cells in purple. The diagonal arrows indicate the next-nearest neighbour interactions, and show why some lattice cells appear twice in equation (S5) (dark purple and dark turquoise).

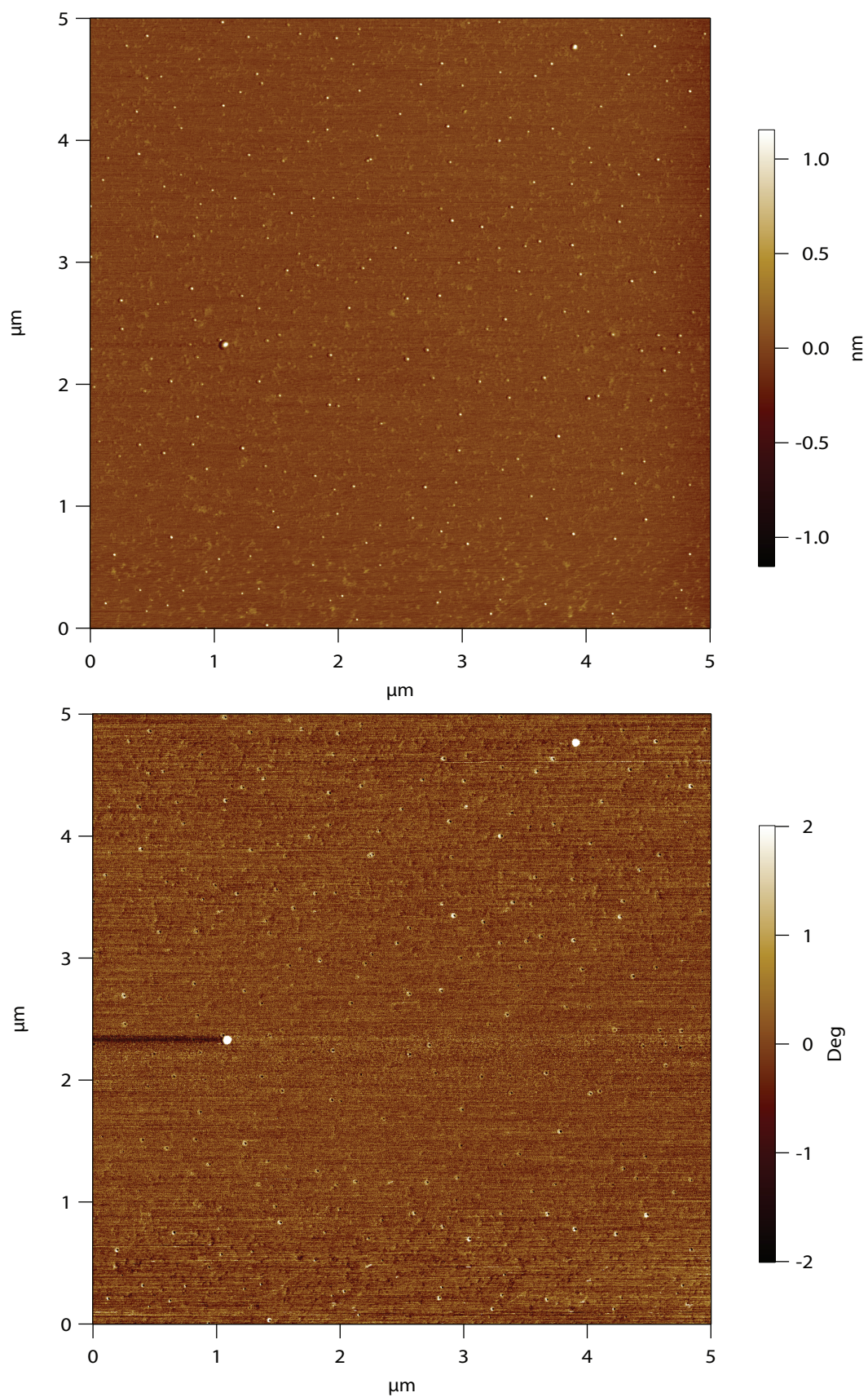


Fig. S4 AFM images of single particles of the polymer depicted in figure 1 (b) of the main text 0.17% coverage: (top) height image; (bottom) phase image. Images have been measured after dropcasting 5 μL of a 0.0025 mg/mL solution of polymer in dioxane on mica.

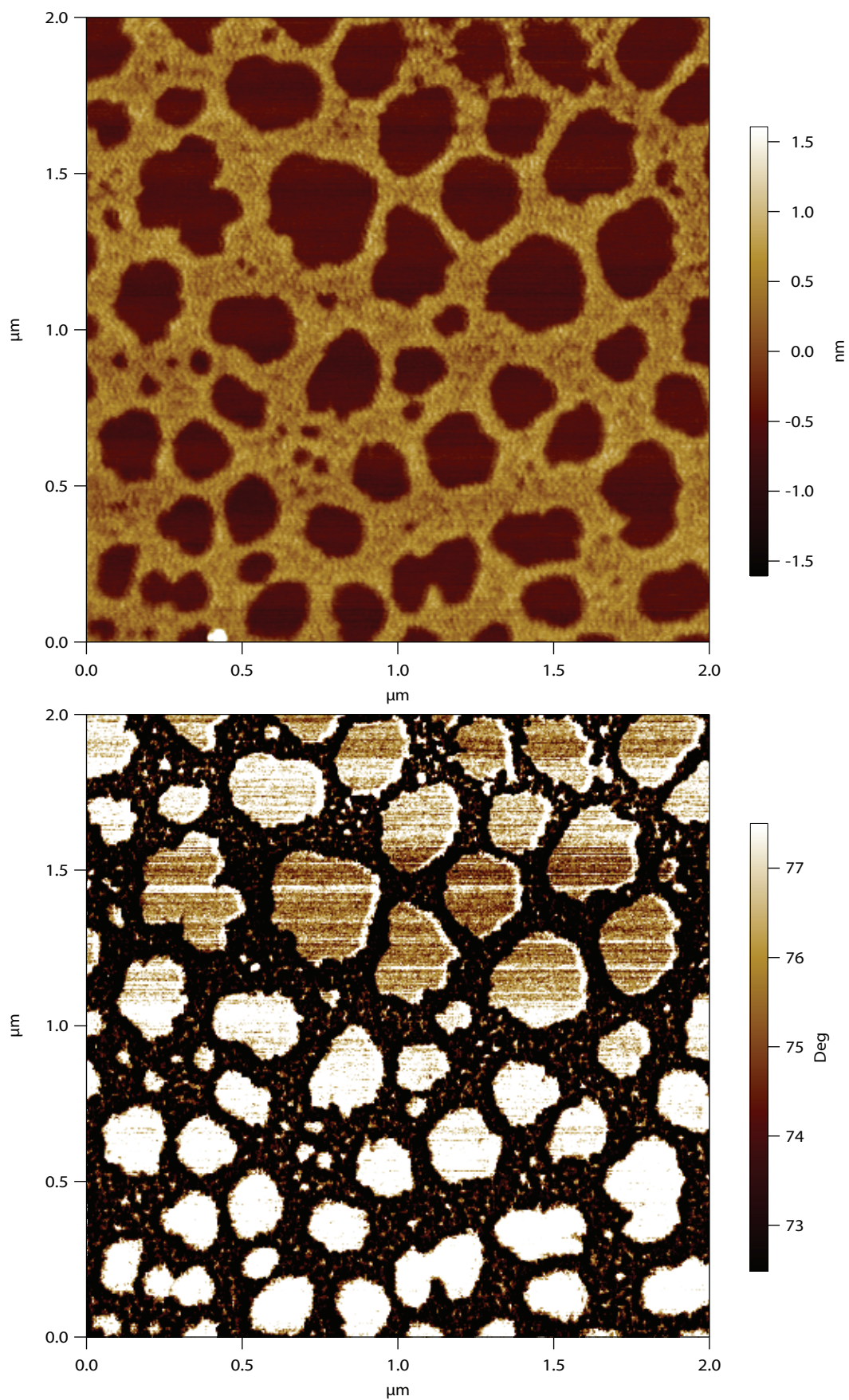


Fig. S5 AFM images of a network formed by aggregation of particles of the polymer depicted in figure 1 (b) of the main text at ~60% coverage: (top) height image; (bottom) phase image. Images have been measured after spin-coating a 0.01 mg/mL solution of polymer in dioxane on mica.

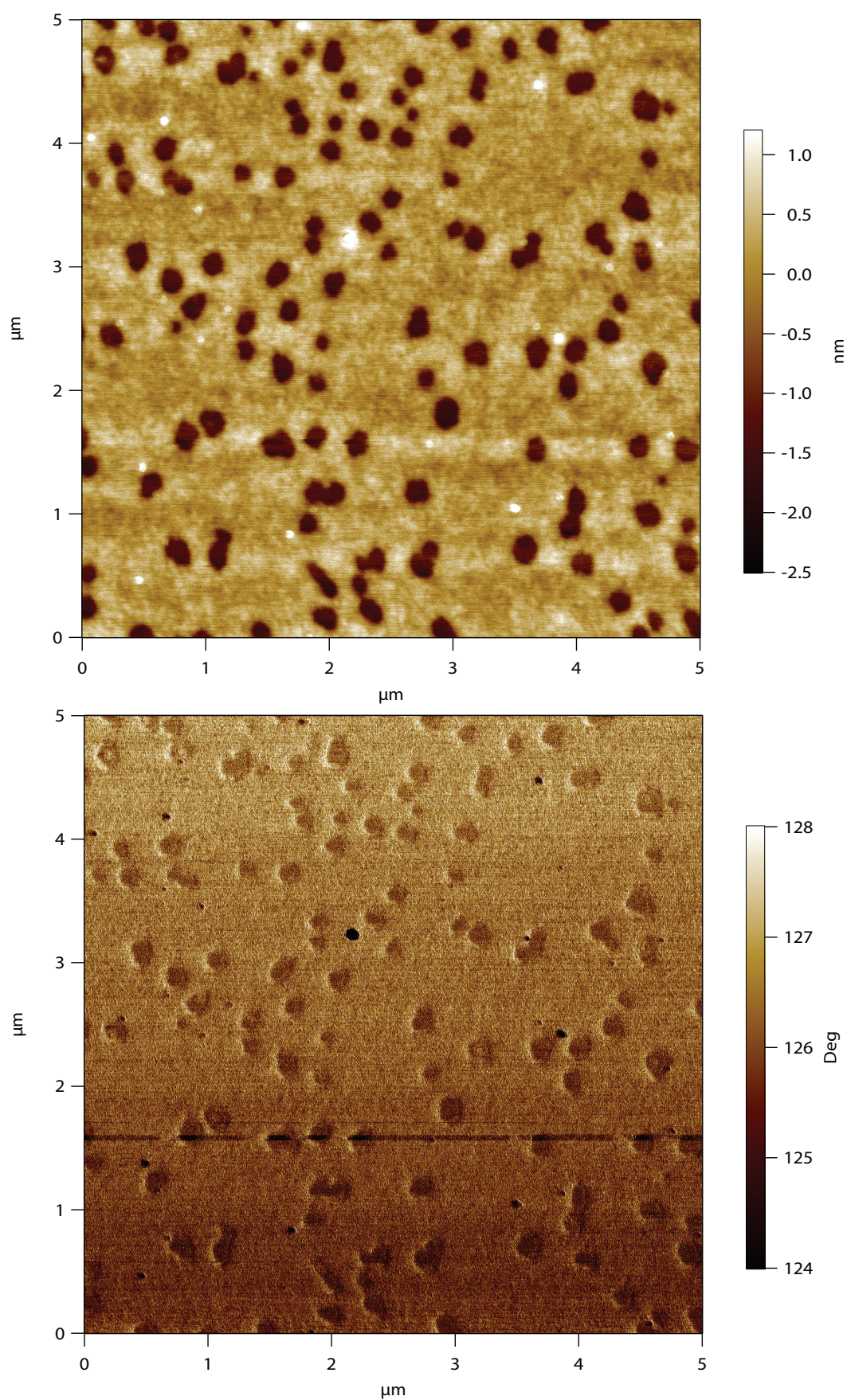


Fig. S6 AFM images of a continuous film with holes formed through close aggregation of particles of the polymer depicted in figure 1 (b) of the main text at $\sim 90\%$ coverage: (top) height image; (bottom) phase image. Images have been measured after dropcasting $10 \mu\text{L}$ of a 0.05 mg/mL solution of polymer in dioxane on mica.

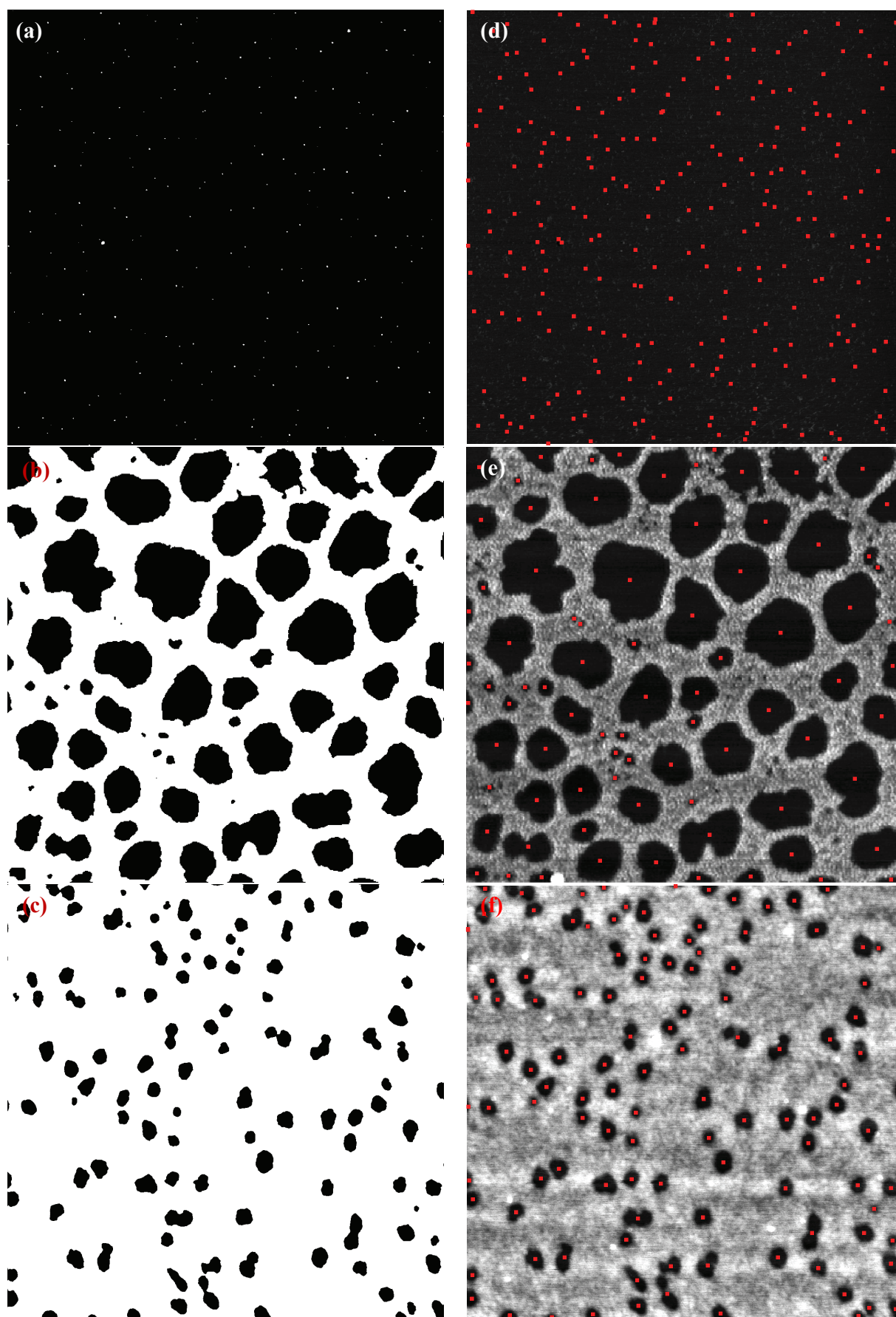


Fig. S7 Binary images obtained by thresholding of the height AFM images: (a) 0.17% coverage; (b) 60% coverage; (c) 90% coverage. Visualisation of the initial germs used in the Minkowski functional square grain growth analysis of the AFM images: (d) 0.17% coverage; (e) 60% coverage; (f) 90% coverage.

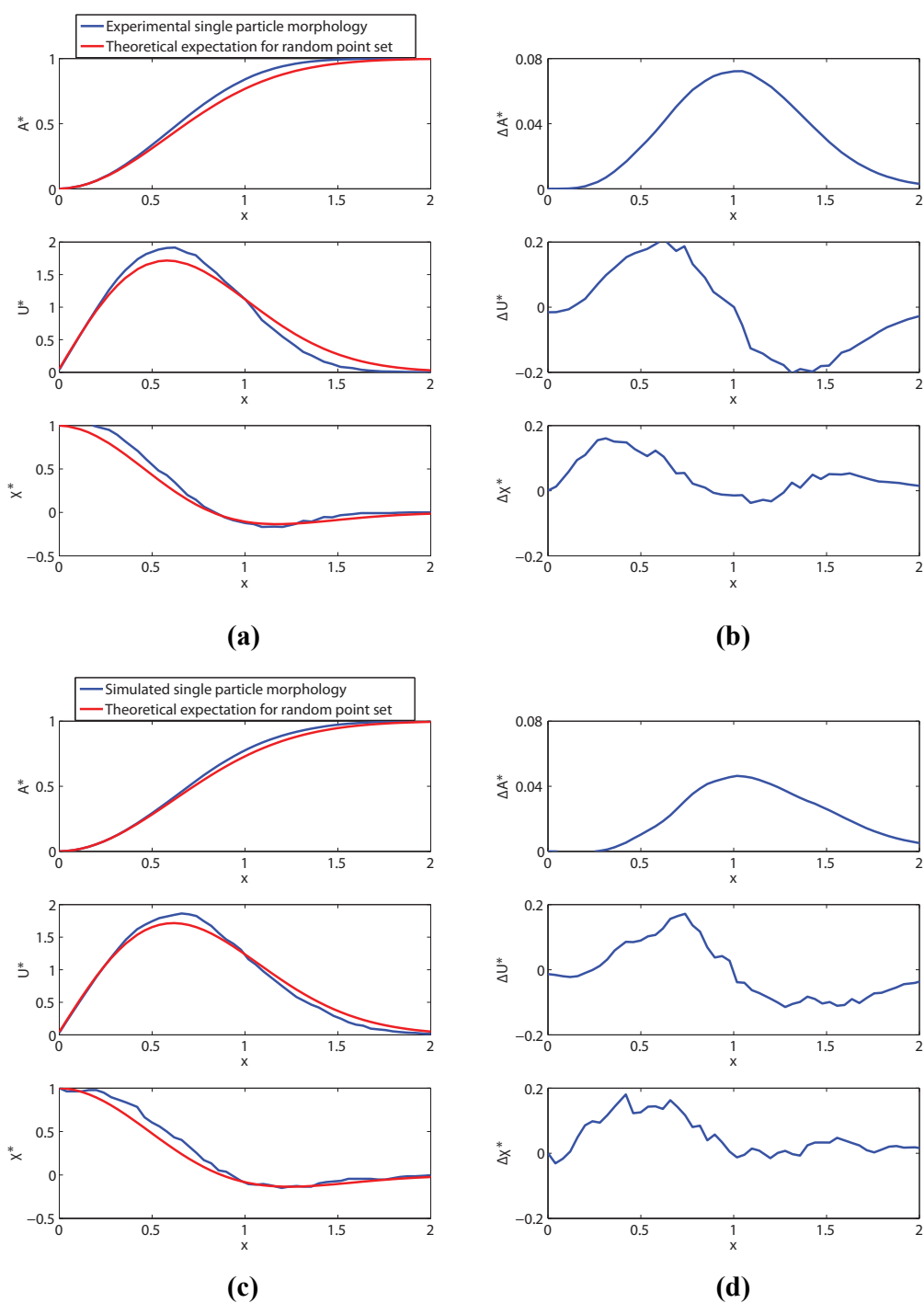


Fig. S8 Minkowski grain growth analysis for the single particle morphologies. (a) Minkowski grain growth analysis performed on AFM image of single particle morphology along with the theoretical expectation for a random point set with the same germ density; (b) Difference of the analysis in (a); (c) Minkowski grain growth analysis performed on simulated image of the single particle morphology along with the theoretical expectation for a random point set with the same germ density; (d) Difference of the analysis in (c).

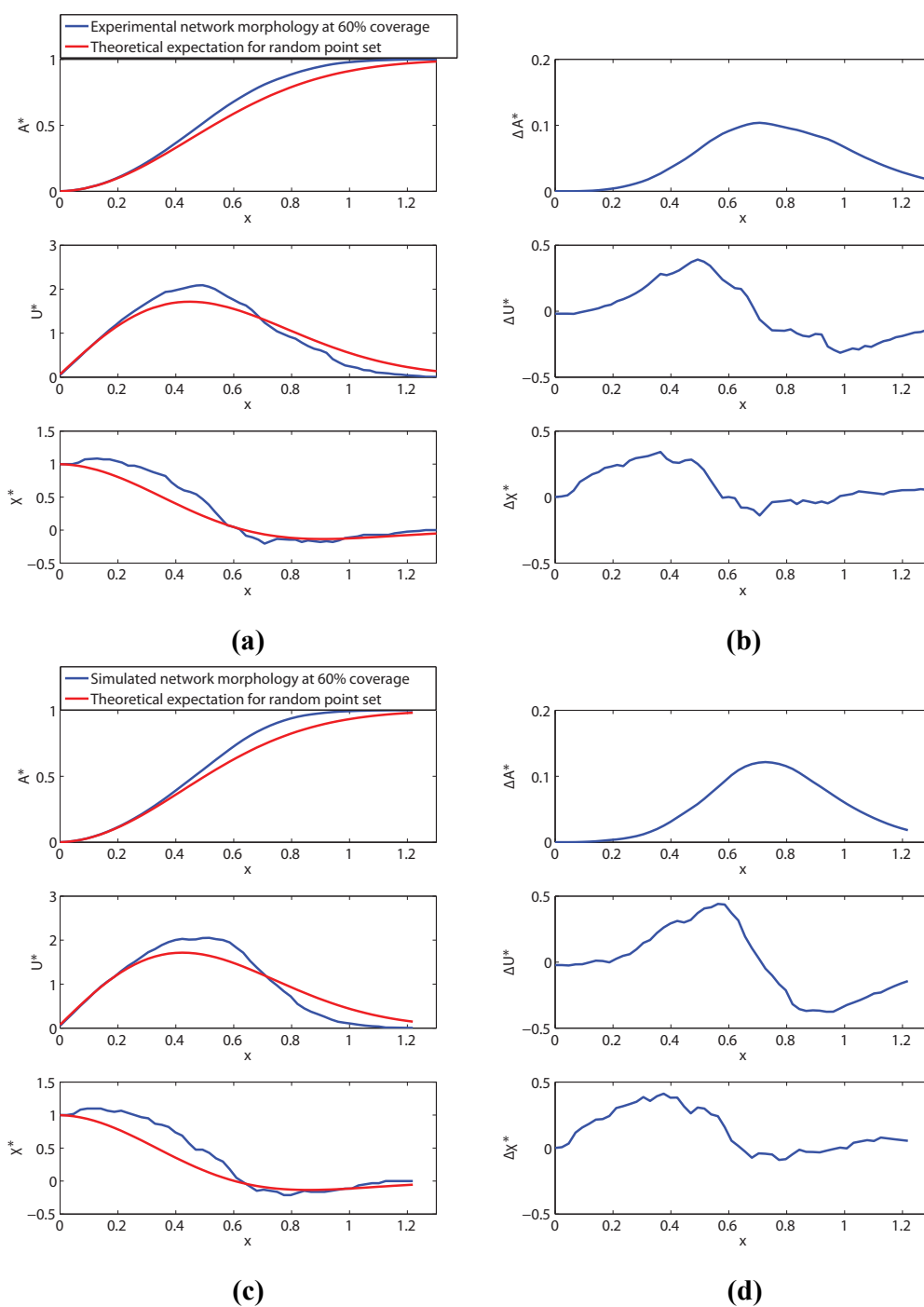


Fig. S9 Minkowski grain growth analysis for the network morphologies at 60% coverage. (a) Minkowski grain growth analysis performed on AFM image of the network morphology along with the theoretical expectation for a random point set with the same germ density; (b) Difference of the analysis in (a); (c) Minkowski grain growth analysis performed on simulated image of the network morphology along with the theoretical expectation for a random point set with the same germ density; (d) Difference of the analysis in (c).

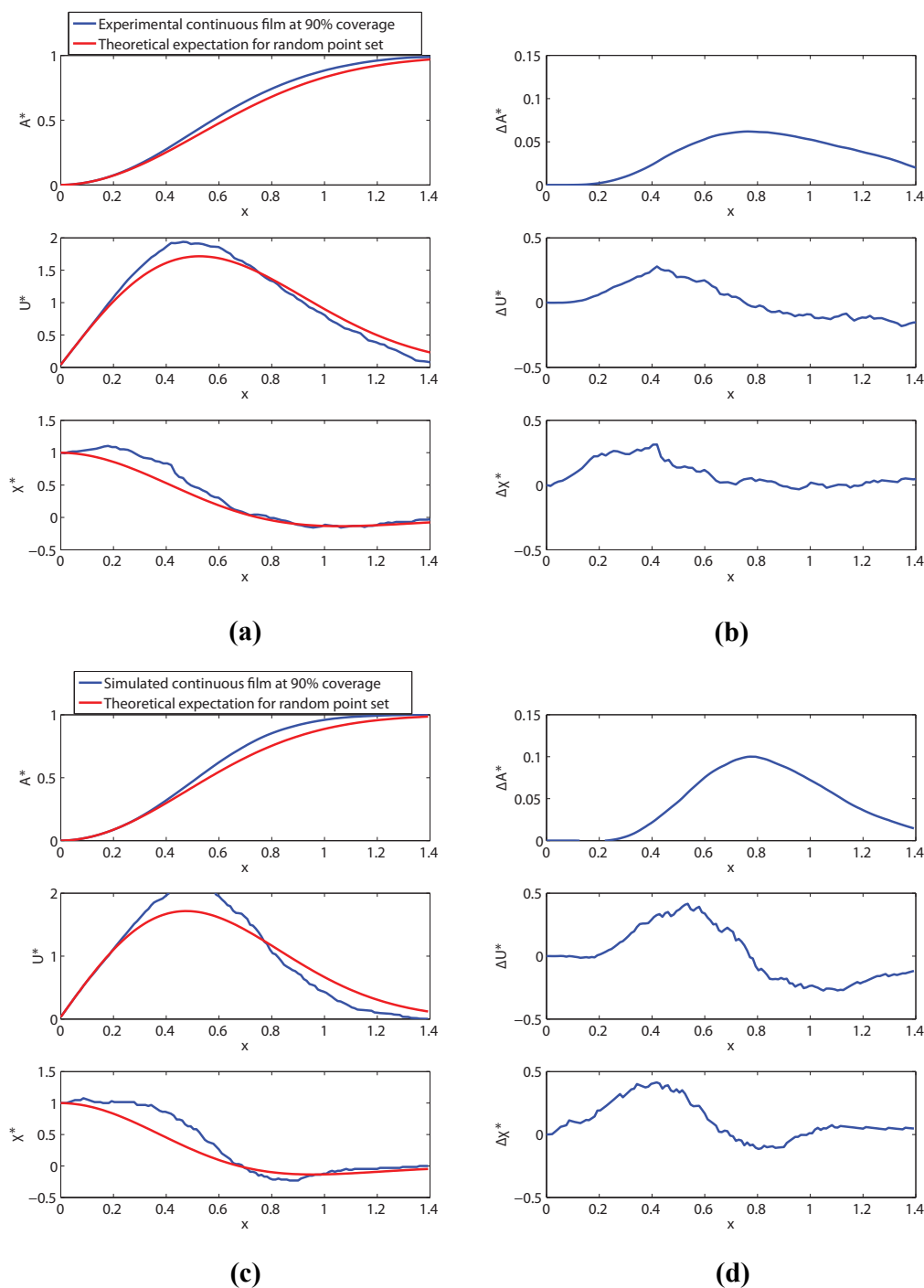


Fig. S10 Minkowski grain growth analysis for the continuous film morphologies at 90% coverage. (a) Minkowski grain growth analysis performed on AFM image of the film morphology along with the theoretical expectation for a random point set with the same germ density; (b) Difference of the analysis in (a); (c) Minkowski grain growth analysis performed on simulated image of the film morphology along with the theoretical expectation for a random point set with the same germ density; (d) Difference of the analysis in (c).